

# Multiscale Phase Inversion of Seismic Marine Data

Lei Fu

King Abdullah University of Science and Technology, Division of Physical Science and Engineering,  
Thuwal 23955-6900, Saudi Arabia

## ABSTRACT

We test the feasibility of using multiscale phase inversion (MPI) of seismic marine data. To avoid cycle-skipping, the multiscale strategy temporally integrates the traces several times, i.e. high-order integration, to produce low-boost seismograms that are used as input data for the initial iterations of MPI. As the iterations proceed, higher frequencies in the data are boosted by using integrated traces of lower order as the input data. Results with synthetic data and field data from the Gulf of Mexico produce robust and accurate results if the model does not contain strong velocity contrasts such as salt-sediment interfaces. Imaging sediments below salt still presents challenges to MPI because of the defocusing of seismic waves below salts. A partial remedy is to employ both source and receiver arrays that focus events below the salt.

amplitudes is a moderate loss in resolution in the velocity tomogram. Sun et al. (1993) demonstrated the feasibility of this method by applying it to synthetic crosswell data.

We now test the MPI strategy on both synthetic and field data for surface seismic data. The resolution of MPI velocity tomograms is further improved by using the MPI tomogram as the starting point for FWI. We also test some strategies for using MPI to update the velocity model below salt with strong velocity contrasts along the salt-sediment boundary.

The next section describes the theory of MPI, which is then followed by the numerical results section. Both synthetic data and field data are inverted with the MPI strategy for sediments with moderate velocity contrasts. Tests on models with salt bodies provide unmet challenges for successful imaging below salt. The final section presents the summary.

## INTRODUCTION

One of the most significant problems with full waveform inversion (FWI) is the cycle-skipping problem (Virieux and Operto, 2009; Warner et al., 2013; Warner and Guasch, 2014), where an iterative solution gets stuck in a local minimum. Another problem is that the amplitudes of the predicted traces do not fully match those of the observed data because all of the actual physics is not used in computing the predicted traces. To remedy both problems, Sun et al. (1993) proposed a multiscale phase inversion (MPI) method. To avoid cycle-skipping, the multiscale strategy temporally integrates the traces several times to produce low-boost seismograms that are used as input data for the initial iterations of MPI. To avoid the necessity of exactly predicting amplitudes, only the phase of the seismic data is predicted and the amplitude information is largely ignored. The penalty in not matching

## THEORY OF MULTISCALE PHASE INVERSION

For phase inversion, we replace the magnitude spectrum of a calculated trace with the magnitude spectrum of the corresponding observed trace so that the amplitude strengths of two traces are equalized. The predicted and observed traces are Fourier transformed to obtain the magnitude spectrum  $A$  and phase spectrum  $\phi$ ,

$$\mathcal{F}[p(\mathbf{g}, t; \mathbf{s})_{cal}] = A(\mathbf{g}, \omega; \mathbf{s})_{cal} e^{i\phi(\mathbf{g}, \omega; \mathbf{s})_{cal}}, \quad (1)$$

$$\mathcal{F}[p(\mathbf{g}, t; \mathbf{s})_{obs}] = A(\mathbf{g}, \omega; \mathbf{s})_{obs} e^{i\phi(\mathbf{g}, \omega; \mathbf{s})_{obs}}. \quad (2)$$

Here,  $\mathbf{s}$  is the location of the source, and  $\mathbf{g}$  is the location of the geophone for a monochromatic source at frequency  $\omega$ . The modified traces  $\bar{p}(\mathbf{g}, t; \mathbf{s})_{cal}$  is obtained by replacing  $A(\mathbf{g}, \omega; \mathbf{s})_{cal}$  with  $A(\mathbf{g}, \omega; \mathbf{s})_{obs}$  and performing the inverse

Fourier transform,

$$\bar{p}(\mathbf{g}, t; \mathbf{s})_{cal} = \mathcal{F}^{-1} \left\{ L(\omega) A(\mathbf{g}, \omega; \mathbf{s})_{new} e^{i\phi(\mathbf{g}, \omega; \mathbf{s})_{cal}} \right\}, \quad (3)$$

$$\bar{p}(\mathbf{g}, t; \mathbf{s})_{obs} = \mathcal{F}^{-1} \left\{ L(\omega) A(\mathbf{g}, \omega; \mathbf{s})_{obs} e^{i\phi(\mathbf{g}, \omega; \mathbf{s})_{obs}} \right\}, \quad (4)$$

where  $A(\mathbf{g}, \omega; \mathbf{s})_{new} = A(\mathbf{g}, \omega; \mathbf{s})_{obs}$  and  $L(\omega)$  is a low-pass filter applied to data.

**Misfit function.** The modified traces are time-integrated and their difference are used for the MPI misfit function,

$$\epsilon^{mpi} = \sum_{\mathbf{s}, \mathbf{g}} \int dt [I^n \bar{p}(\mathbf{g}, t; \mathbf{s})_{cal} - I^n \bar{p}(\mathbf{g}, t; \mathbf{s})_{obs}]^2, \quad (5)$$

where  $I^n$  is an integration operator  $I \equiv \int dt$  performed  $n$  times, and  $\bar{p}(\mathbf{g}, t; \mathbf{s})_{cal}$  and  $\bar{p}(\mathbf{g}, t; \mathbf{s})_{obs}$  are the modified traces in equations (3) and (4). If we set  $A(\mathbf{g}, \omega; \mathbf{s})_{new} = A(\mathbf{g}, \omega; \mathbf{s})_{cal}$  in equation (3), then the MPI misfit function becomes that for full wave inversion, except that the traces have been shaped by the filter  $L(\omega)$  and integration operator.

Figure 1a1 shows the predicted trace  $p_{cal}$  with one reflection event, the observed trace with three reflection events  $p_{obs}$  is shown in Figure 1a2, and the corresponding modified predicted and observed traces are shown in Figures 1a3 and a4, respectively. Figures 1b1-b4 show the predicted, observed, modified predicted, and modified observed traces with one integration, respectively. We can see the wavelet is a Gaussian wavelet. Figures 1c1-c4 show the predicted, observed, modified predicted, and modified observed traces with twice forward integration, respectively. The source wavelet here is a heaviside function.

For the twice integrated observed and calculated traces, the area under them is roughly proportional to the traveltimes. So the difference between two traces is proportional to the difference between the observed and calculated traveltimes. In this sense, we can say that MPI is a form of wave equation travelttime inversion.

**Gradient.** The gradient of MPI misfit function  $\epsilon^{mpi}$  w.r.t. the velocity field  $c(\mathbf{x})$

$$\begin{aligned} \gamma^{mpi}(\mathbf{x}) &= \frac{\partial \epsilon^{mpi}}{\partial c(\mathbf{x})} \\ &= \frac{1}{c(\mathbf{x})^3} \sum_{\mathbf{s}} \int dt [I^n \dot{\bar{p}}(\mathbf{x}, t; \mathbf{s})] [I^n \dot{\bar{p}}'(\mathbf{x}, t; \mathbf{s})], \end{aligned} \quad (6)$$

where dot means time differentiation,  $\bar{p}(\mathbf{x}, t; \mathbf{s})$  is the pressure wavefield by the source at  $\mathbf{s}$ , and  $\bar{p}'(\mathbf{x}, t; \mathbf{s})$  is the wavefield computed by backprojecting the seismogram residual (Luo and Schuster, 1991)  $\delta \bar{p}$ ,

$$\bar{p}'(\mathbf{x}, t; \mathbf{s}) = \sum_r g(\mathbf{x}, -t; \mathbf{g}, 0) * \delta \bar{p}, \quad (7)$$

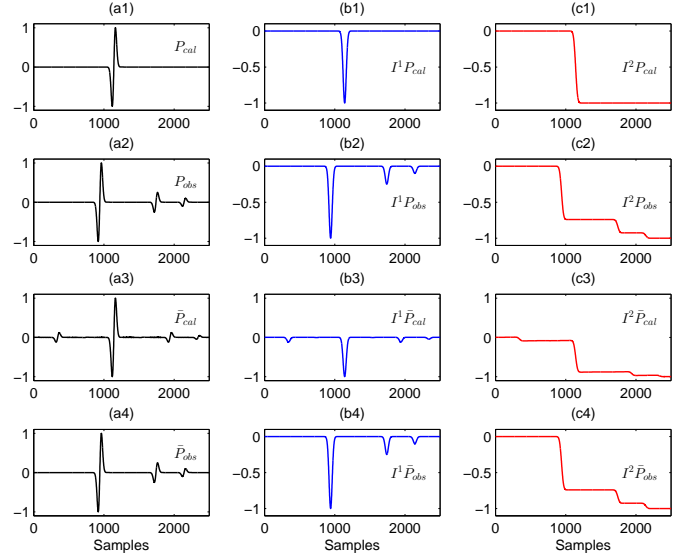


Figure 1: The original data without integration, a1) predicted, a2) observed, a3) modified predicted, and a4) modified observed traces. The traces with once ( $n = 1$ ) integration are in b1 - b4, and twice ( $n = 2$ ) integration are in c1 - c4.

with

$$\delta \bar{p} = \bar{p}(\mathbf{g}, t; \mathbf{s})_{obs} - \bar{p}(\mathbf{g}, t; \mathbf{s})_{cal}. \quad (8)$$

In theory, the integration operator  $I^n$  on the fields  $\bar{p}$  and  $\bar{p}'$  in equation 6 can be alternatively applied to source functions that generate them without changing the misfit gradient. For example,  $I^n \dot{\bar{p}}(\mathbf{x}, t; \mathbf{s})$  is equivalent to generating a wavefield using source with  $I^{n-1}$  integrations.

For comparison, the traditional full wave inversion (FWI) gradient is

$$\begin{aligned} \gamma^{fwi}(\mathbf{x}) &= \frac{\partial \epsilon^{fwi}}{\partial c(\mathbf{x})} \\ &= \frac{1}{c(\mathbf{x})^3} \sum_{\mathbf{s}} \int dt [\dot{p}(\mathbf{x}, t; \mathbf{s})] [\dot{p}'(\mathbf{x}, t; \mathbf{s})], \end{aligned} \quad (9)$$

where the FWI gradient is the dot product between the source forward wavefield and backprojected wavefield with the data residual  $\delta p = p(\mathbf{g}, t; \mathbf{s})_{obs} - p(\mathbf{g}, t; \mathbf{s})_{cal}$ .

Figure 2 shows the comparison of gradients for the FWI and MPI methods. Figure 2a is the true model, Figure 2b is the initial model and the sources and receivers are evenly distributed on the surface. We use a 15-Hz first-order derivative of the Gaussian function as the wavelet. Figure 2c shows the FWI gradient at the first iteration, and Figures 2d-f depict the MPI gradient with different orders of integrations applied to the traces at the first iteration. If no integration is applied to these traces, the MPI gradient is quite similar to the FWI gradient. When the  $n = 2$  integrations operator is applied to the traces, the MPI gradient provides low wave-number information about the model, and the higher wave-number model in-

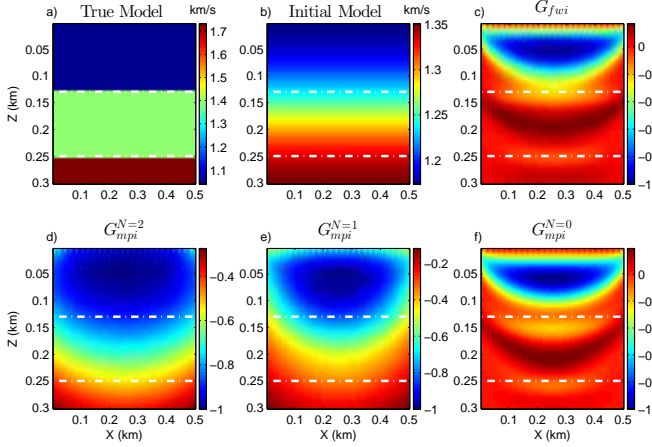


Figure 2: a) The true model, b) initial model, c) FWI gradient. The MPI gradients with d)  $n = 2$ , e)  $n = 1$ , and f)  $n = 0$  integrations of traces. The white dashed lines indicate the layer interfaces.

formation will be gradually incorporated as  $n$  decreases to zero for the MPI method.

**Frequency multiscale strategy.** The data should be band-pass filtered into different frequency bands with different peak frequencies, and then the FWI or MPI method is used at the early iterations and then high-frequency data at later iterations. A low-pass Wiener filter (Boonyasirivat et al., 2009) can be computed by

$$L_{wiener}(\omega) = \frac{W_{target}(\omega)W_{original}^{\dagger}(\omega)}{|W_{original}(\omega)|^2 + \epsilon^2}, \quad (10)$$

where,  $L_{wiener}(\omega)$  is the Wiener filter,  $W_{original}(\omega)$  is the original wavelet,  $W_{target}(\omega)$  is the target wavelet,  $\dagger$  denotes complex conjugate,  $\omega$  is the the angular frequency, and  $\epsilon$  is a damping factor to prevent numerical instability.

One formula for choosing optimal frequency bands proposed by Sirgue and Pratt (2004) is

$$f_{n+1} = \frac{f_n}{\alpha_{min}}, \quad (11)$$

where  $f_n$  is the current frequency,  $f_{n+1}$  is the next frequency to be chosen, and  $\alpha_{min} = z/\sqrt{h^2 + z^2}$  is the parameter that depends on the maximum half offset  $h$  and the maximum depth  $z$  to be imaged.

**Workflow of MPI.** To avoid local minima, the MPI multiscale strategy (Sun and Schuster, 1993) temporally integrates the traces  $N$  times to produce low-boost seismograms that are used as input data for the initial iterations. These low-boost traces are inverted for several iterations until the decrease in residual ( $\theta$ ) is below a specified threshold ( $\theta_1$ ). Then the data are high boosted by using the  $N - 1$  integrated traces as the input data and the low-boosted tomogram as the new starting model. When the integration order is  $n = 0$  and the data residual falls

below a specified threshold, the data will be moved to the next higher frequency band and the MPI procedure is repeated. See the dashed box in the MPI workflow shown in Figure 3.

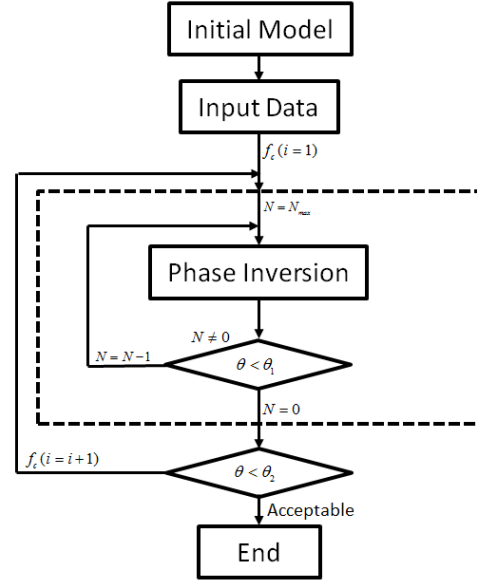


Figure 3: The multiscale phase inversion workflow. Here,  $N$  is the integration number,  $N_{max}$  is the maximum integration number,  $f_c$  is the centre frequency of the low-pass filter,  $\theta_1$  and  $\theta_2$  are predefined threshold.

## NUMERICAL RESULTS

To demonstrate the effectiveness of MPI and its advantages, we invert two synthetic data from the Marmousi and 2D SEG/EAGE salt models, and marine data from the Gulf of Mexico. The modeling kernels are based on the constant-density acoustic wave equation, while the observed input data are generated by solving the constant-density acoustic wave equation (Alford et al., 1974), viscoacoustic equation (Operto et al., 2007) or elastic equation (Levander, 1988) in the synthetic cases.

### Marmousi Model

The Marmousi model (Figure 4) is discreted into 243x767 grids with spacing of 10 m in both direction. There are 192 sources with interval of 40 m and 383 receivers with interval of 20 m located along the free surface.

	1	2	3	4	5	6
$f_c$ (Hz)	2.1	3.8	7.2	13.4	24.9	46.6

Table 1: Different peak frequencies of the bandpass filters applied to the Marmousi synthetic data, where  $f_c$  represent the centre frequency.

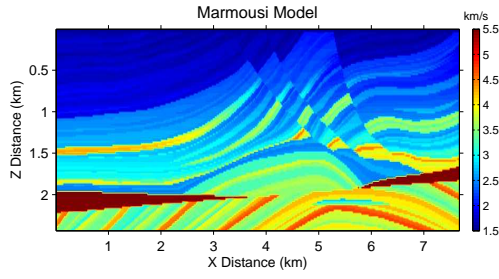


Figure 4: The Marmousi model

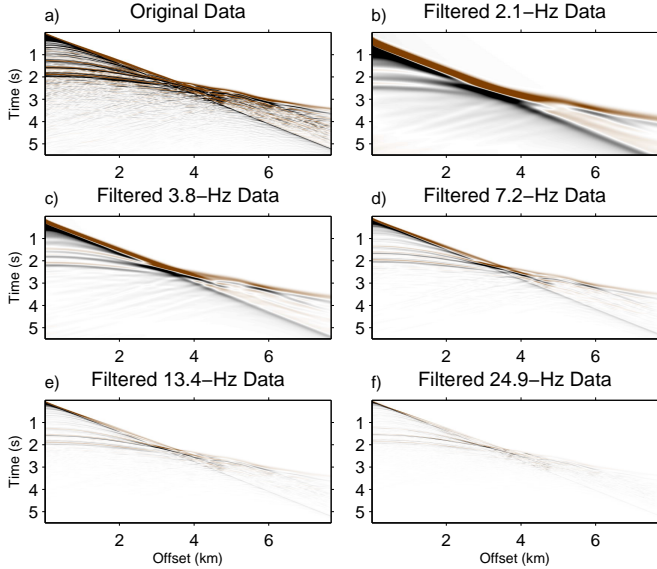


Figure 5: Synthetic acoustic data from the Marmousi model: a) the original data filtered with the peak frequencies of b) 2.1-Hz, c) 3.8-Hz, d) 7.2-Hz, e) 13.4-Hz, and f) 24.9-Hz.

Acoustic Data

The original acoustic data are generated by solving the constant density acoustic equation with a 15-Hz first-order derivative of a Gaussian wavelet. A common shot gather for the source at  $x = 0$  m is shown in Figure 5a. Different bandpass filters (table 1) are applied to the original data, and the filtered data are shown in Figures 5b-f. For the frequency multiscale strategy, low-frequency data are inverted at an early stage, which provides low wave-number model information. Higher frequency data are gradually incorporated at later stages, which provide the detailed high wave-number information about the model. The frequency multiscale strategy is used for both the FWI and MPI methods.

Figure 6a is the smoothed initial velocity model with a velocity error of 12%, and Figure 6b is the  $v(z)$  initial velocity model with a velocity error of 22%. The FWI and MPI tomograms with the smoothed initial model (Figure 6a) are shown in Figures 6c and 6e. The FWI and MPI tomograms with the  $v(z)$  initial model (Figure 6b) are shown in Figures 6d and 6f. Figure 7 shows the veloc-

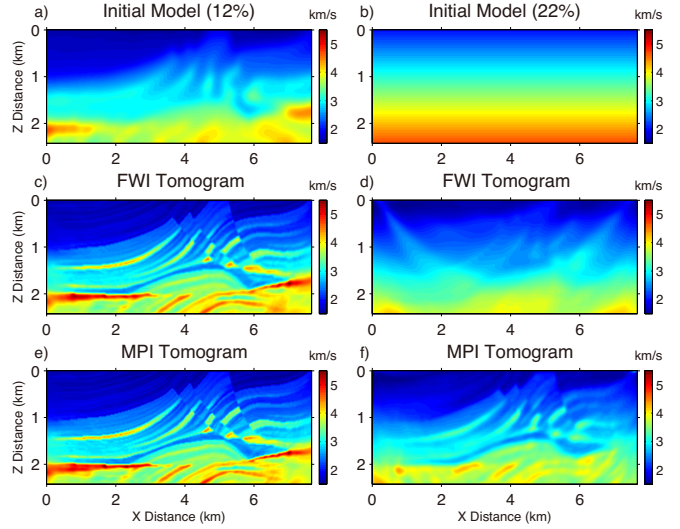


Figure 6: Inversion results for acoustic data. a) The smoothed initial velocity model with velocity error of 12%, c) multiscale FWI and e) MPI tomograms based on a), b) the  $v(z)$  initial velocity model with the velocity error of 22%, d) multiscale FWI and f) MPI tomograms based on b) .

ity profile comparison for the true, initial, FWI and MPI velocity models at different positions.

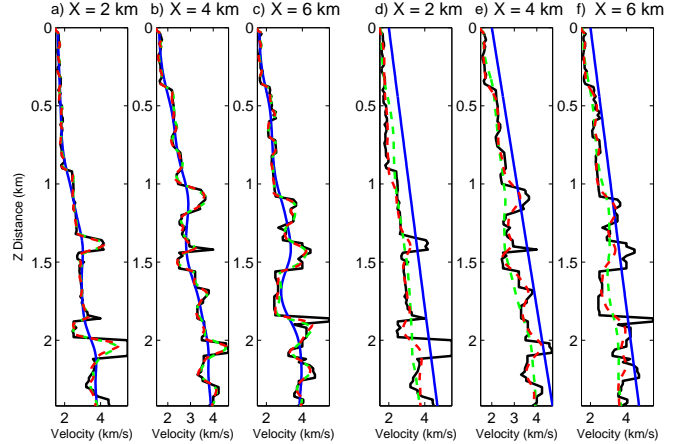


Figure 7: Velocity profile (in Figure 6) comparison, for true, smooth initial (12%), FWI and MPI tomogram at, a)  $x = 2$  km, b)  $x = 4$  km, c)  $x = 6$  km; for true,  $v(z)$  initial (22%), FWI and MPI tomogram at, d)  $x = 2$  km, e)  $x = 4$  km, f)  $x = 6$  km. Where the black, blue, green and red curves represent the true, initial, FWI and MPI tomogram.

We can see that both the FWI and MPI tomograms have a good agreement with the true model when the initial model is not far away from the true model. However, when the initial model is far away from the true model, traditional FWI gets stuck to a local minimal, while MPI can provide an accurate tomogram. Thus, the MPI method has a more robust convergence than FWI for

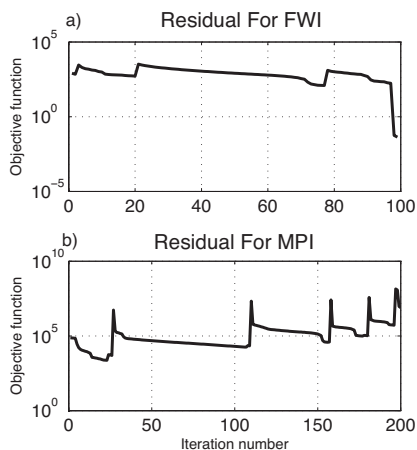


Figure 8: Data residual at different iterations in semilog plot, for the a) multiscale FWI and b) MPI methods.

this model.

Figure 8 shows the data residual at each iteration for the FWI and MPI methods when the smoothed initial model (Figure 6a) is used. The original data is filtered into 6 different frequency bands here, so there are 6 stages of convergence for both methods. In addition, the maximum integration number  $N_{max} = 2$  gradually decreases to 0 for each frequency band in the MPI method. The computational cost of MPI is slightly larger than that of FWI because of the integration operations.

### Visco-acoustic Data

We now use visco-acoustic data as input traces to the acoustic FWI and MPI algorithms. The goal is to test the sensitivity of each method to the unmodeled attenuation effects in the data. The visco-acoustic data are generated by solving visco-acoustic equations, where the source wavelet and acquisition geometry are the same as in the acoustic case. A pressure source is injected in the water, and the pressure field is recorded. The true  $v_p$  model is shown in Figure 4 and the  $Q$  model is shown in Figure 9, where the minimum  $Q$  is 25. The visco-acoustic data for the shot location at  $x = 0$  is shown in Figure 10b, we can see that reflections and refractions are highly attenuated due to the highly attenuative medium. The amplitude of the visco-acoustic traces are quite different from those in acoustic data (Figure 10a).

We apply the acoustic FWI and MPI methods to these synthetic visco-acoustic data, where the initial  $v_p$  model is shown in Figure 11a. The FWI and MPI tomograms are shown in Figures 11b and 11c, respectively, where the velocity profile comparison at different offset locations are shown in Figure 12. It is found that both the FWI and MPI tomograms in deep area are not accurately inverted. However, the MPI tomogram is more accurate than that in the FWI tomogram at shallow area. The likely reason is that the MPI method is less sensitive than the FWI

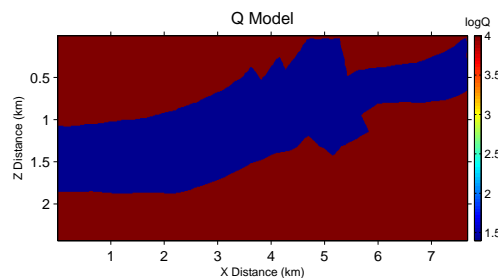


Figure 9: The  $Q$  model used to generate the visco-acoustic data, the  $Q$  value is plotted in a logarithm scale.

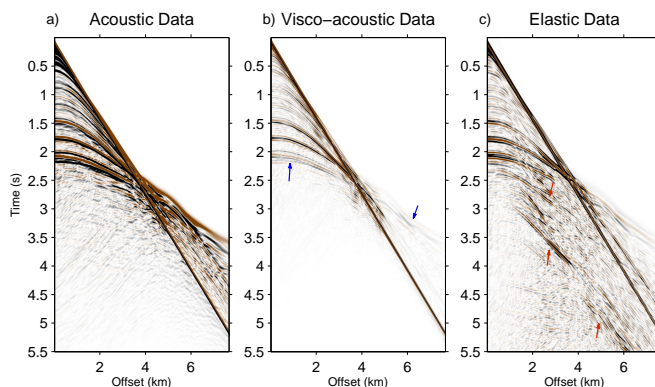


Figure 10: Synthetic seismic data, a) constant density acoustic data, b) visco-acoustic data, and c) elastic data, for the shot location at  $x = 0$  km. All subplots have the same colorbar.

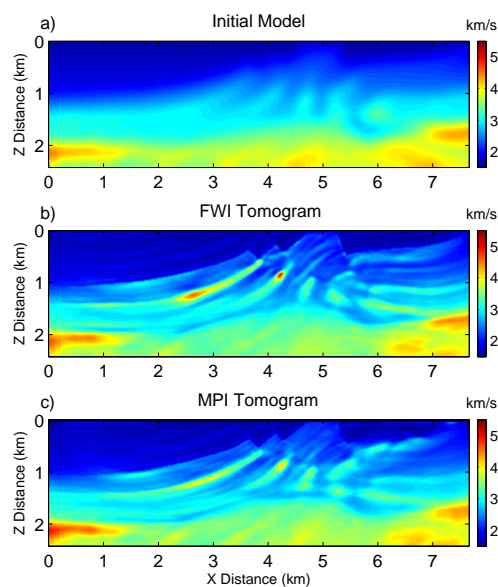


Figure 11: Inversion results for visco-acoustic data. a) The initial  $v_p$  model, b) FWI, and c) MPI tomogram.

method in accurately computing amplitudes.

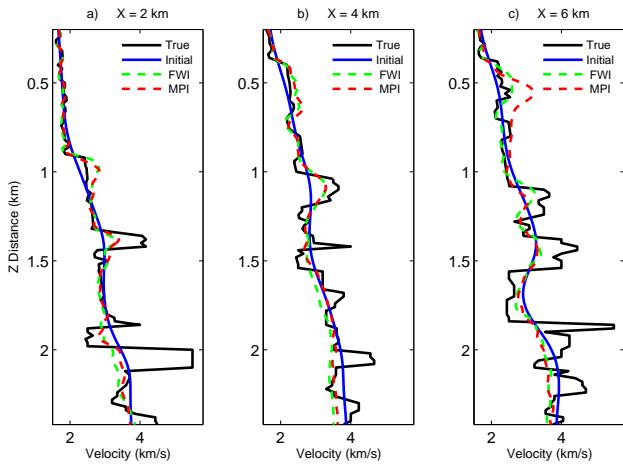


Figure 12: Velocity profile (in Figure 11) comparison between the true model, initial model, FWI and MPI tomogram at a)  $x = 2$  km, b)  $x = 4$  km, and c)  $x = 6$  km.

### Elastic Data

We now use elastic data as input traces to the acoustic FWI and MPI algorithms. The goal is to test the sensitivity of each method to the unmodeled elastic effects in the data. The elastic data are generated by solving the elastic wave equation, where the source wavelet and acquisition geometry are the same as in the acoustic case. The pressure is injected in the water and the pressure field is recorded as the negative of the average of the normal stresses. The true  $v_p$  model is shown in Figure 4, the density is given by  $\rho = 0.31v_p^{0.25}$ , and  $v_s = v_p/\sqrt{3}$ , except the shear velocity of the ocean water is set to 0 m/s. The elastic data at shot location  $x = 0$  is shown in Figure 10c, where the three red arrow indicate the converted 'PSP' arrivals.

The FWI and MPI tomograms are shown in Figure 13b and 13c, respectively, and the corresponding velocity profiles are shown in Figure 14. We can see that the MPI tomogram is noticeably more accurate than the FWI tomogram.

## 2D SEG/EAGE Salt Model

The 2D SEG/EAGE Salt Model is shown in Figure 15a, which is discretized into  $440 \times 1350$  grids with a gridpoint spacing of 5 m in both direction and the sea bottom is at the depth of around 250 m. There are 338 sources with a shot interval of 20 m and the 676 receivers are located every 10 m located just below the free surface. The original data are generated by solving the acoustic equation with a 20-Hz Ricker wavelet.

The initial model is a  $v(z)$  model with 1500 m/s at the top and linearly increasing to 2600 m/s at the bottom. The MPI tomogram is shown in Figure 15b. On one hand, we can see the top boundary of the salt body mostly agrees with the true model, however, the bottom boundary is far from the true model. Although the inverted velocity

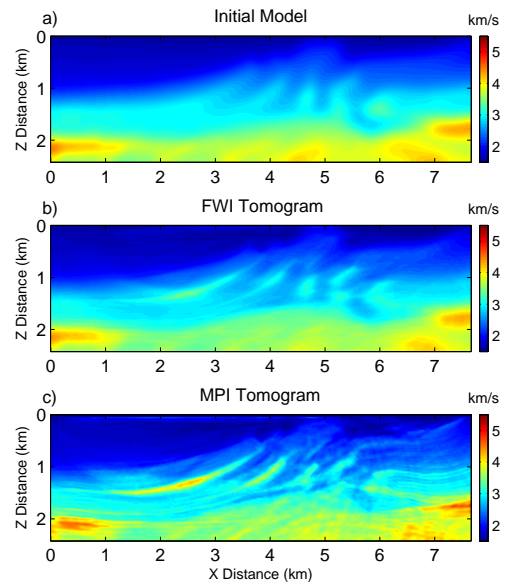


Figure 13: Inversion results for elastic data. a) The initial  $v_p$  model, b) FWI tomogram and c) MPI tomogram.

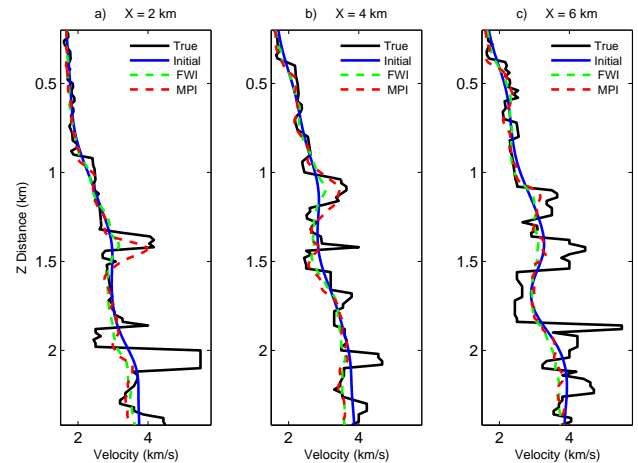


Figure 14: Velocity profile (in Figure 13) comparison between the true model, initial model, FWI tomogram and MPI tomogram at a)  $x = 2$  km, b)  $x = 4$  km, and c)  $x = 6$  km.

above the top boundary agrees well with the true model, the salt-body velocity is much smaller than the true salt velocity.

In order to improve the velocity tomogram shown in Figure 15b, a flooding technique (Boonyasiriwat et al., 2010) is used. The top salt boundary is picked from the tomogram, and the true salt velocity of 4480 m/s is used to flood the region beneath the top boundary, and the resulting tomogram is shown in Figure 16a. The RTM image (Figure 16b) is obtained based on the salt-flood velocity (Figure 16a), and the salt-body boundary (the black curve indicated) is picked from the RTM image. Combining the picked salt-body boundary and the MPI tomogram in Figure 15b, we can obtain the sediment-flood velocity

model (Figure 16c). The sediment-flood velocity model is used as the initial velocity model for the MPI, and finally the MPI tomogram is shown in Figure 15c. The comparison of velocity profiles at different locations for the true model, initial model, MPI tomogram without flood technique, and MPI tomogram with flood technique are shown in Figure 17. The flooding technique improves the accuracy of the the salt-body tomogram, however, accurately inverting the area beneath salt bottom is still a challenge.

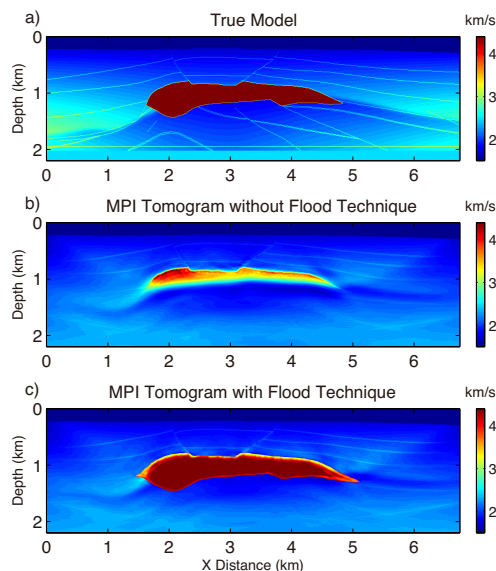


Figure 15: Inversion results for the 2D SEG/EAGE salt model. a) The true model, b) MPI tomogram without flood technique, and c) MPI tomogram with flood technique.

## Gulf of Mexico Data

The MPI method is applied to a streamer data set from the Gulf of Mexico, which was acquired using 515 shots with a shot interval of 37.5 m, a time-sampling interval of 2 ms, a recording time of 10 s, and 480 hydrophones per shot. The hydrophone interval is 12.5 m, with the minimum and maximum source-receiver offsets of 198 m and 6 km, respectively.

Prior to applying FWI and MPI to this marine data set, we apply the following 4 data preprocessing steps:

- Transform the original data from 3D to 2D format by applying the filter  $\sqrt{i/\omega}$  in the frequency domain to correct for 3D geometrical spreading (Zhou et al., 1995).
- Mute the noise before the first arrivals, the attenuation factor  $Q$  is estimated by the spectral ratio method (Maresh et al., 2006), and the attenuation effect is compensated by applying an inverse- $Q$  filter to the data.
- Re-sample the data with the new sampling interval of 0.5 ms.

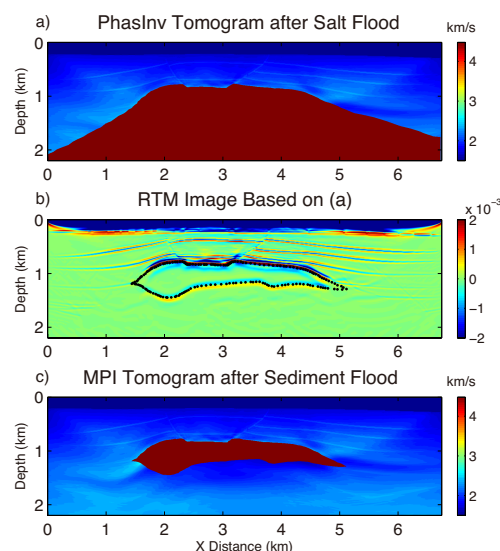


Figure 16: Flooding produce and MPI images. a) Velocity model obtained after a salt flood of the MPI tomogram shown in Figure 15b, b) RTM image based on the salt-flood velocity tomogram in a), where the black curve indicates the salt-body boundary we picked, and c) velocity model obtained after a salt and sediment flood.

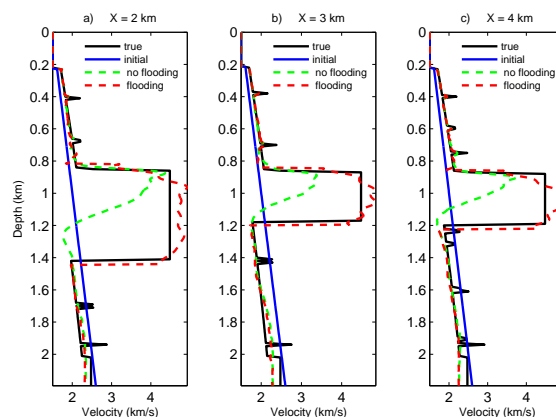


Figure 17: Velocity profile comparison for the true model, initial model, MPI tomogram without flood, and MPI tomogram with flood at a)  $x = 2$  km, b)  $x = 3$  km, c)  $x = 4$  km. The black, blue, green and red curves represent the true model, initial model, MPI tomogram without flood technique and MPI tomogram with flood technique.

- The source wavelet is estimated by stacking along water-bottom reflections, and the resulting wavelet is shown in Figure 18a, and the spectrum is shown in Figure 18b. The dominant frequency is around 16 Hz.

The original data are filtered into different frequency bands with the different centre filters dis-layed in table 2. The low-frequency data are inverted in the early iterations, and then higher frequency data are gradually incorporated into the later iterations. The  $v(z)$  velocity model shown in Figure 19a is used as the initial model for the

	1	2	3	4	5	6
$f_c$ (Hz)	3.3	6.5	9.5	13.5	18.5	32.5

Table 2: Peak frequencies of different bandpass filters applied to the Gulf of Mexico marine data, where  $f_c$  represent the centre frequency.

multiscale FWI and MPI. The initial model is discretized into 800x6012 grids with a grid spacing of 3.125 m in both directions.

Figures 19b and 19c depict the FWI tomogram after 21 iterations and MPI tomogram after 35 iterations, respectively. Both the FWI and MPI tomograms have a higher resolution compared with the initial velocity model. In addition, the resolution of the MPI tomogram is slightly higher than that seen in the FWI tomogram. In order to verify the reconstructed FWI and MPI tomograms, we compare the migration images and angle domain common image gathers (ADCIGs).

The original data are migrated using reverse time migration (RTM) based on the initial velocity model, the FWI tomogram and the MPI tomogram, and the migration images are shown in Figures 20a, 20b, and 20c, respectively. The corresponding ADCIGs are shown in Figures 21a, 21b and 21c, respectively. Using either the FWI or MPI tomograms as the migration velocity, the resulting migration images are better focused than that obtained by using the initial velocity model. We see that the RTM images computed with the FWI and MPI tomograms are quite similar.

Comparing the ADCIGs, we can see that the CIGs associated with the FWI and MPI tomograms are flatter than those from the initial velocity model. As for deep region on the right, the CIGs show curved events which means the migration velocity is less accurate in this region.

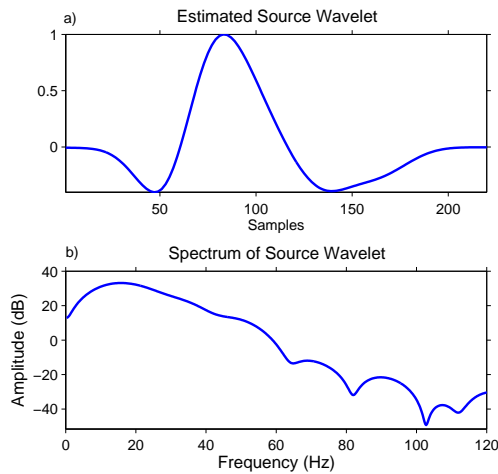


Figure 18: a) Estimated source wavelet, and b) the spectrum of the source wavelet.

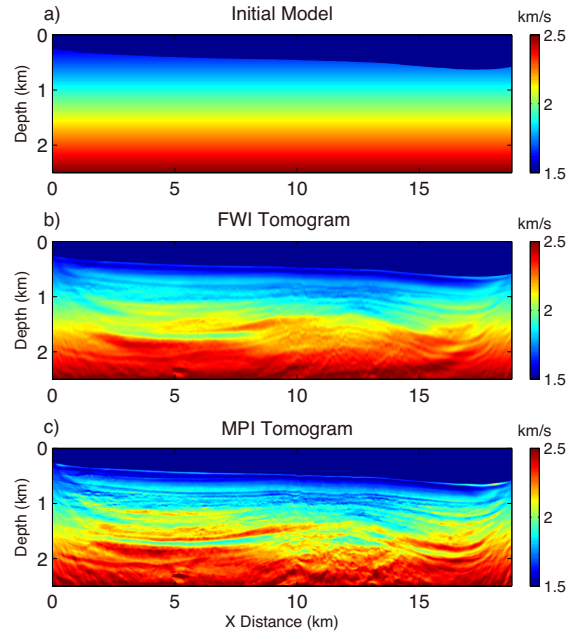


Figure 19: Inversion results from the Gulf of Mexico marine data. a) The  $v(z)$  initial model, b) multiscale FWI, and c) multiscale MPI tomogram.

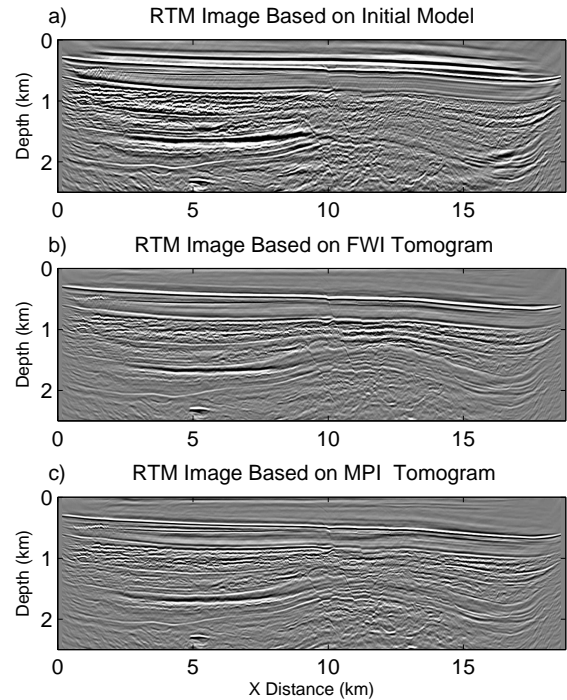


Figure 20: RTM migration images from the marine data that uses the migration velocity from a) the initial model, b) FWI tomogram, and c) MPI tomogram.

## DISCUSSION AND CONCLUSION

The multiscale strategy temporally integrates the traces several times to produce low-boost seismograms that are used as input data for the initial iterations of MPI. The area under the integrated traces are roughly proportional

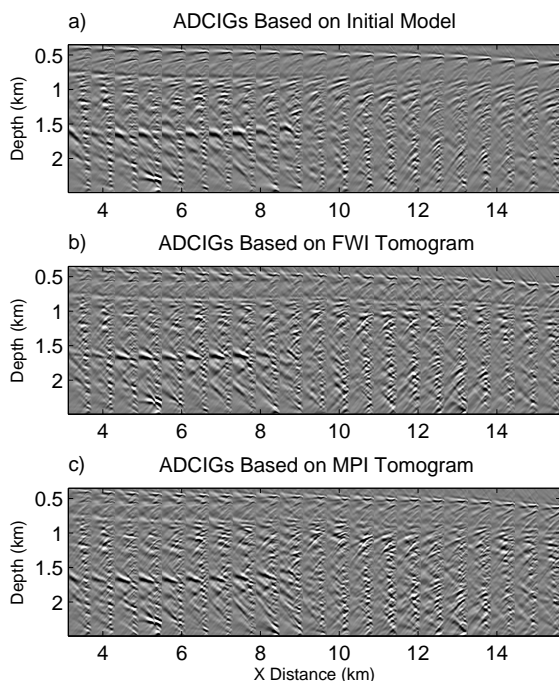


Figure 21: Angle domain common image gathers (ADCIGs) based on a) the initial model, b) FWI tomogram, and c) MPI tomogram.

to the traveltimes, which means the MPI is a form of wave equation traveltime inversion without requiring traveltime picking. In addition, the amplitude differences are largely ignored in the MPI objective function.

Synthetic examples show that both the MIP and FWI methods can obtain similar tomograms when the initial velocity model is not far away from the true model. However, the MPI method provides for a more accurate tomogram than FWI when the initial model is far from the true model. Meanwhile, MPI can obtain more accurate tomograms than FWI for inverting the visco-acoustic and elastic data. Synthetic examples show that MPI is more robust than FWI for inverting seismic marine data.

In the marine data case, both the FWI and MPI methods successfully inverted the marine data set to obtain tomograms that are more accurate than the initial velocity model. However, the MPI tomogram has slightly higher resolution than that of FWI tomogram. Comparing the RTM images, it is found that the quality of the migration image based on the MPI tomogram is quite similar to that of the FWI tomogram.

## ACKNOWLEDGMENTS

The research reported in this publication was supported by the King Abdullah University of Science and Technology (KAUST) in Thuwal, Saudi Arabia. We are grateful to the sponsors of the Center for Subsurface Imaging and Modeling (CSIM) Consortium for their financial support. For computer time, this research used the resources of the Supercomputing Laboratory at KAUST and the IT Re-

search Computing Group. We thank them for providing the computational resources required for carrying out this work.

## REFERENCES

- Alford, R., K. Kelly, and D. M. Boore, 1974, Accuracy of finite-difference modeling of the acoustic wave equation: *Geophysics*, **39**, 834–842.
- Boonyasiriwat, C., G. T. Schuster, P. Valasek, and W. Cao, 2010, Applications of multiscale waveform inversion to marine data using a flooding technique and dynamic early-arrival windows: *Geophysics*, **75**, R129–R136.
- Boonyasiriwat, C., P. Valasek, P. Routh, W. Cao, G. T. Schuster, and B. Macy, 2009, An efficient multiscale method for time-domain waveform tomography: *Geophysics*, **74**, WCC59–WCC68.
- Levander, A. R., 1988, Fourth-order finite-difference p-sv seismograms: *Geophysics*, **53**, 1425–1436.
- Luo, Y., and G. T. Schuster, 1991, Wave-equation travel-time inversion: *Geophysics*, **56**, 645–653.
- Operto, S., J. Virieux, P. Amestoy, J.-Y. L'Excellent, L. Giraud, and H. B. H. Ali, 2007, 3d finite-difference frequency-domain modeling of visco-acoustic wave propagation using a massively parallel direct solver: A feasibility study: *Geophysics*, **72**, SM195–SM211.
- Sirgue, L., and R. G. Pratt, 2004, Efficient waveform inversion and imaging: A strategy for selecting temporal frequencies: *Geophysics*, **69**, 231–248.
- Sun, Y., G. T. Schuster, et al., 1993, Time-domain phase inversion, *in* SEG Technical Program Expanded Abstracts 1993: Society of Exploration Geophysicists, 684–687.
- Virieux, J., and S. Operto, 2009, An overview of full-waveform inversion in exploration geophysics: *Geophysics*, **74**, WCC1–WCC26.
- Warner, M., and L. Guasch, 2014, Adaptive waveform inversion-fwi without cycle skipping-theory: Presented at the 76th EAGE Conference and Exhibition 2014.
- Warner, M., T. Nangoo, N. Shah, A. Umpleby, and J. Morgan, 2013, Full-waveform inversion of cycle-skipped seismic data by frequency down-shifting, *in* SEG Technical Program Expanded Abstracts 2013: Society of Exploration Geophysicists, 903–907.